JGR Atmospheres

RESEARCH ARTICLE
10.1029/2020JD033647

Special Section:
A NEW ERA OF LIGHTNING OBSERVATIONS FROM SPACE

GPM-DPR Observations on TGFs Producing Storms

A. Tiberia[1], F. Porcú[2], M. Marisaldi[3,6], M. Tavani[4], J. Lapierre[5], A. Ursi[4], F. Fuschino[6], L. P. D'Adderio[1], and S. Dietrich[1]

[1]Institute for Atmospheric Science and Climate, ISAC-CNR, Rome, Italy, [2]Department of Physics and Astronomy, University of Bologna, Bologna, Italy, [3]Birkeland Centre for Space Science, Department of Physics and Technology, University of Bergen, Bergen, Norway, [4]INAF-IAPS, National Institute for Astrophysics, Rome, Italy, [5]Earth Networks, Germantown, Maryland, USA, [6]INAF-OAS, National Institute for Astrophysics, Bologna, Italy

Abstract Unique spaceborne measurements of the three-dimensional structure of convective clouds producing terrestrial gamma ray flashes (TGFs) were performed using both active and passive microwave sensors on board the Global Precipitation Measurement (GPM)-Core Observatory satellite, finding coherent features for nine TGF-producing storms. The delineation of cloud structure using the radar reflectivity factor shows convective cells with significant vertical development and thick layers with high ice content. Compared to other cumulonimbus clouds in the tropics, the TGFs counterparts have higher reflectivity values above 3 and 8 km altitude showing in all cases a cumulonimbus tower and the TGFs locations are very close, or coincident, to these high *Z* columns, where reflectivity exceeds 50 dBz. Using the GPM Microwave Imager radiometer, most thunderstorms show a very strong depression of polarization corrected temperature (PCT) at channel 89 GHz, indicating a strong scattering signal by ice in the upper cloud layers. At channel 166 GHZ, the difference between vertical and horizontal brightness temperature signal always returns positive values, from 0.2 up to 13.7 K indicating a complex structure with randomly/vertically oriented ice particles. The PCT was used to characterize the analyzed storms in terms of hydrometeor types, confirming in 7/9 cases a high likelihood of hail/graupel presence. To perform analysis on the TGFs parent flashes, radio atmospherics data from the Earth Networks Total Lightning Network lightning network were used. Waveform data indicate that all cases are intra-cloud events and TGFs typically take place during the peak of flash rate production. Finally, the analysis of the most intense event is shown.

Key Point:
- High-energy radiation from thunderclouds

Supporting Information:
Supporting Information may be found in the online version of this article.

Correspondence to:
A. Tiberia,
a.tiberia@isac.cnr.it

Citation:
Tiberia, A., Porcú, F., Marisaldi, M., Tavani, M., Lapierre, J., Ursi, A., et al. (2021). GPM-DPR observations on TGFs producing storms. *Journal of Geophysical Research: Atmospheres*, *126*, e2020JD033647. https://doi.org/10.1029/2020JD033647

Received 5 AUG 2020
Accepted 16 FEB 2021

Author Contributions:
Conceptualization: A. Tiberia, F. Porcú, M. Marisaldi, M. Tavani, J. Lapierre, S. Dietrich,
Data curation: A. Tiberia, F. Porcú, M. Marisaldi, J. Lapierre
Formal analysis: A. Tiberia, J. Lapierre
Funding acquisition: S. Dietrich
Methodology: A. Tiberia, F. Porcú, M. Marisaldi, M. Tavani, J. Lapierre, L. P. D'Adderio, S. Dietrich
Supervision: A. Tiberia, F. Porcú, M. Marisaldi, M. Tavani, J. Lapierre, A. Ursi, F. Fuschino, L. P. D'Adderio, S. Dietrich
Writing – review & editing: A. Tiberia, F. Porcú, M. Marisaldi, M. Tavani, J. Lapierre, A. Ursi, F. Fuschino, L. P. D'Adderio, S. Dietrich

1. Introduction

Terrestrial gamma ray flashes (TGFs) are sub-millisecond bursts of high-energy photons that were first observed from space in 1994 by the Compton Gamma Ray Observatory (Fishman et al., 1994) later associated with positive intra-cloud (IC) discharges (Shao et al., 2010; Stanley et al., 2006; E. Williams et al., 2006) and extensively observed by the Reuven Ramaty High Energy Solar Spectroscopic Imager (RHESSI; Smith et al., 2005), Astrorivelatore Gamma a Immagini LEggero (AGILE; Marisaldi et al., 2010; Tavani et al., 2009), Fermi Gamma-ray Burst Monitor (GBM; Briggs et al., 2013) and the Atmosphere-Space Interactions Monitor (Østgaard et al., 2019).

It remains still unknown why not all the thunderstorms produce gamma-ray bursts and if there are favorable characteristics and physical conditions that produce TGFs within thunderstorms. In order to understand which conditions are favorable to the development of these events several studies are focused on the structures that mainly define the characteristics of clouds, both at macro and micro-scale (Splitt et al., 2010). performed the first meteorological comparison of TGFs and associated thunderstorms using Tropical Rainfall Measuring Mission (TRMM) Microwave Imager (TMI) combined with geostationary satellite observations. They found that such TGFs Producing Thunderstorms (hereafter TPT) have cloud top values ranging from 13.6 to 17.3 km, consistent with the theoretical estimates (source altitude between 15 and 21 km) previously found by Dwyer and Smith (2005). In a recent study Larkey et al. (2019) found that, the interflash time interval prior to a TGF-producing flash was 24% longer than the mean interflash interval suggesting that larger than average thunderstorm charging period, therefore higher large-scale electric field are necessary for TGFs production.

More recently, regions of frequent TGFs emissions are compared to lightning detections from the Lightning Imaging Sensor (LIS; Christian et al., 1999) on board the TRMM. In Barnes et al. (2015), two samples were created, storms with TGF and storms without TGF, based on whether RHESSI detected a TGF in the region. The TRMM Microwave Instrument (TMI; Wentz et al., 2001) was used to compare the hydrometeor content of the storms within the two samples. Despite the limitations due to the TGF location uncertainties, the very likely presence of multiple cell storms in the field of view, and the evolution of the event in a such large range of time, clear differences in the hydrometeor content of the two samples were found. The TGFs regions contained higher concentrations of cloud water and ice and precipitation water and ice.

Detailed meteorological observations of TPT detected by Fermi were given by Chronis et al. (2016). They analyzed 24 Fermi TGFs within the next generation weather radars weather radar network operational range. By studying the Enhanced Echo Top radar product, they show how TGFs are more correlated with high altitude regions in a storm. The Vertical Integrated Liquid Density, reflectivity (Z) and Convective Available Potential Energy values, taken from the National Centers for Environmental Prediction North American Regional Reanalysis, show that these TGFs originate from storms having a wide range of convective strengths, without any clear common characteristics. These results are confirmed also by the recent study of Ursi (2019) that linked TGFs production to cloud instantaneous and dynamical features as extracted by visible-infrared geostationary satellite sensors. The present study takes advantage of the availability of satellite borne radar data to perform analysis from a new perspective, overcoming most of the limitations affecting ground based weather radar observation (e.g., attenuation, beam blocking, and anomalous propagation), and extending the coverage to oceans and desert areas.

The launch of the NASA/JAXA Global Precipitation Measurement (GPM) mission (Hou et al., 2014), opens a new era in cloud studies from space. The constellation of satellites has now reached an optimal configuration, ensuring a 3-hourly global coverage of passive microwave sensors, and is now completed by the GPM Core Observatory (GPM-CO), successfully launched in February 2014. The GPM core satellite is equipped with the GPM Microwave Imager (GMI) and Dual-frequency Precipitation Radar (DPR). In particular, respect to pre-existing sensors, they both bring a number of interesting new capabilities, such as, for the GMI, the improved ground resolution and the additional high frequency channels (166 H/V). This provides information on mid-tropospheric humidity and frozen hydrometeors. The double frequency of the DPR, designed to improve knowledge of precipitation processes with higher sensitivity with respect to the single-frequency (Ku-band) radar used in TRMM, is designed to provide greater dynamic range, more detailed information on microphysics (D'Adderio et al., 2018, 2019; Marra et al., 2017), and better accuracies in rainfall retrievals (Iguchi et al., 2002; Panegrossi et al., 2016; Petracca, 2018; Speirs et al., 2017).

The aim of this work is to provide information on the structure of the TPT by means of active and passive microwave innovative sensors on board GPM-CO. The main characteristics of these storms are retrieved and vertical profiles of reflectivity and the horizontal structure of Brightness Temperatures (TB) are studied around the site of the detected TGF. The acronym more frequently use in this study are reported in the related list.

2. Instruments and Data Sets

In this study, the database was built by searching for GPM-CO overpasses over the area of TGFs occurrence, finding nine cases of TPT observed by DPR and GMI. In particular, TGF data collected by AGILE and Fermi and simultaneous observations by the Earth Networks Total Lightning Network (ENTLN; Liu & Heckman, 2011; Rudlosky, 2015) and by the GPM, are analyzed.

2.1. TGFs

The TGF events considered in this work were detected by the Mini CALorimeter (MCAL; Marisaldi et al., 2014) on board the Astrorivelatore Gamma ad Immagini LEggero AGILE (Tavani et al., 2009) and by the GBM aboard the Fermi Gamma-ray Space Telescope (Briggs et al., 2013). AGILE is a mission of the Italian Space Agency (ASI) dedicated to gamma-ray astrophysics, operating since 2007 in a low inclination (2.5°) and Low-Earth Orbit (LEO) at 540 km altitude. The MCAL (Fuschino et al., 2011; Labanti et al., 2009; Marisaldi et al., 2010) is based on scintillating bars for the detection of gamma rays in the range 300 keV–

100 MeV. Fermi detects TGFs from a nearly circular orbit of 565 km altitude with a 25.6° inclination. The GBM, designed for astrophysical observations of gamma-ray transients, consists in 14 scintillation detectors of two types to cover the energy range from 8 keV to 40 MeV (Meegan et al., 2009; Tierney et al., 2013). The detectors are powered off during the spacecraft's transit through the South Atlantic Anomaly region due to the high activity of charged particles. The data from AGILE, include 278 TGFs from the 3rd AGILE TGF catalog (Lindanger et al., 2020; Maiorana et al., 2020) between March 23, 2015 and April 14, 2018. The first Fermi catalog (Roberts et al., 2018) include 1,314 terrestrial gamma ray flashes, detected since launch in July 11, 2008 through July 31, 2016.

We consider only events with associated lightning stroke detected by the World-Wide Lightning Location Network (WWLLN) data set (WWLLN; http://wwlln.net).

The associated stroke provides an estimate of the source location with about 20 km spatial resolution.

2.2. Lightning

With its more than 70 sensors (Hutchins et al., 2012), WWLLN detects Very Low Frequency radio waves over a range of about 3–30 kHz, emitted by Cloud-to-Ground (CG) and a non-negligible fraction of IC lightning strokes with a localization accuracy of about 20 km.

WWLLN is able to detect only strokes with peak current over 30 kA, and therefore, since CG strokes typically have higher peak currents than IC strikes, the network is biased toward CG strokes (Virts et al., 2013). Given the known lower sensitivity of WWLLN to IC lightning and to the relatively low accuracy in the location of the event, our analysis was completed using also the ENTLN, with the twofold aim to improve the lightning location accuracy from 15–20 to less than 5 km and to validate the WWLLN observation.

The ENTLN with its 1,800 globally distributed sensors (frequency from 1 Hz to 12 MHz; Bui et al., 2015; Zhu et al., 2017), has the privilege on detecting Total lightning (IC + CG) useful for applications of thunderstorms monitoring, such as severe weather events and tornadoes (Liu & Heckman, 2011; Rudlosky, 2015).

ENTLN location accuracy is globally below 5 km (Bui et al., 2015), down to 215 m (Zhu et al., 2017) in most favorable cases. The detection efficiency in Florida, the most sensitive area of the network, reaches 97% for CG strokes (Zhu et al., 2017), and 100% for peak currents higher than 25 kA (Mallick et al., 2015).

Comparisons between ENTLN data and TRMM-LIS data are shown in (Rudlosky, 2015) and GLM data are shown in (Marchand et al., 2019). Comparative performance study of the ENTLN and WWLLN can be found in (Bui et al., 2015).

The ENTLN archives the raw waveforms from all its individual sensors, allowing an unprecedent in-depth study of single events, when the characteristics of the lightning sferics is required.

The characteristics of the lightning recorded by ENTLN includes: time accurate to nanoseconds, location in geographical coordinates, flash type classification (CG-IC), peak current, and polarity. Furthermore, it is also possible to determine the maximum distance detected by sensors by manually inspecting the raw waveform data. In case of IC events, the production altitude in the atmosphere can be additionally estimated directly from the time-of-arrival calculations.

2.3. Thunderclouds

Thunderstorms originate in the lower troposphere when moist and warm air is lifted by local thermodynamic instability and becomes buoyant with respect to the surrounding air. Water vapor phase transitions release a huge amount of latent heat within the rising air mass, increasing its upward speed and allowing growth and vertical transport of a wide range of different hydrometeors. This strong vertical current (with typical velocity around few tens of meters per second) lasts until the environment supplies water vapor, and in the more intense cases, and is vertically limited by a strongly stable layer (the tropopause). Heavy rainfall, hailfall, lightning and strong and turbulent air fluxes are usually generated by such convective cloud systems.

Remote sensing instruments are of two primary types, active and passive. Radiometers are passive instruments capable of measuring the power emitted by a body with high accuracy. In particular, they are designed to derive profiles of temperature and water vapor by sounding the atmosphere at multiple frequencies around the absorption lines. The relatively high frequencies employed, make them sensitive to scattering by liquid and frozen hydrometeors. On the other hand, for active remote sensing, radars provide their own source of energy to illuminate the objects they observe, emitting radiation in the direction of the target to be investigated. The signal returned to the receiver provides a measure of the interacting media through the backscattering from that media. Depending on its design, radars can measure the distance from the media and the amount and relative size of the particles in the media. The advantage is their ability to sense information on the location and size distribution of cloud particles. Essentially, they provide a detailed vertical distribution of the precipitation particles in the cloud. There is also sensitivity to the liquid versus frozen particles in the cloud.

The platform from where we observed the storm structure and characteristics is the GPM-CO satellite that operates in a circular, non-sun-synchronous orbit at 407 km altitude, with an inclination of 65° to monitor the same geographic area about two times per day (Hou et al., 2014). The two instruments onboard (GMI radiometer and DPR radar, passive and active instruments, respectively), and their main innovations are presented.

2.3.1. Passive Sensor

The GMI onboard GPM-CO constellation is a state-of-the-art radiometer, with high spatial resolution and a complete set of channels (from 10.6 to 183.7 GHz), over a wide scanning area of 931 km, co-aligned with the swath of DPR (i.e., the strip of the earth's surface from which the data are collected). In particular, GMI offers the most complete set of microwave frequencies available today from space, with 10 dual polarization window channels at 10.6, 18.7, 36.5, 89, and 166 GHz, and three single polarization water vapor absorption channels (one at 23.8 GHz and two at 183.31 GHz).

As a conical scanner, GMI provides passive microwave measurements with the highest available spatial resolution among the GPM constellation of radiometers (i.e., up to roughly 4×7 km at 89 GHz and around 19×32 km at 10.6 GHz). Moreover, it is the only sensor with the double polarization (vertical and horizontal) on the 166 GHz channel, specific for ice detection. Given the correlation between the ice content and lightning production inside clouds (Jayaratne et al., 1983; Takahashi, 1978), the ability to provides information on frozen hydrometeors presence and crystals orientation by this channel is particularly useful for this analysis.

2.3.2. Active Sensor

The DPR onboard the GPM constellation is the second space-borne precipitation radar ever deployed, after the Precipitation Radar (PR), launched on the TRMM satellite in November 1997. It consists of one Ku-band (13.6 GHz) and one Ka-band (35.5 GHz) radar, designed to be operated for simultaneous observation.

One of the reasons for adding the Ka-band frequency channel is to provide a more accurate estimate of the phase-transition height in precipitating systems and thus allowing a better description of solid precipitations (Iguchi et al., 2002). Since the Ku-band channel of the DPR is very similar to the TRMM PR, the principal challenge in the development of the DPR algorithms is to combine the Ka-band and Ku-band data to achieve the objectives mentioned above. The swath widths of Ka- and Ku-band radars: 120 and 245 km, respectively, while both Ka- and Ku-band footprints are of 5.2 km diameter with a vertical resolution of 125 m (Iguchi et al., 2002). The DPR operates in three scanning modes: Normal scan (NS), matched scan and high sensitivity scan. Outputs can be in single-frequency in the outer part of the swath, covered only by Ku-band radar or double-frequency in the inner part of the swath, observed by both radars, depending to the scanning mode: MS footprints collect simultaneous measurement at Ka- and Ku-band providing outputs from double-frequency based algorithm (Iguchi et al., 2002).

Table 1
Resume of TGF and Lightning Features for the Data Set Considered

ID	Data	Local time (h)	Counts	Lon (deg)	Lat (deg)	Type	Dist. foot (km)	*i* (kA)	*d* (km)	Height (km)	Δt (min)
#1F	2014-07-01	17:33	11	−84.9585	7.4813	IC	403	+50	6,000	15	+11
#2F	2014-08-18	03:35	11	26.7369	1.3223	IC	39	–	–	–	−06
#3F	2014-09-11	09:04	20	88.4148	25.5771	IC	216	+86	5,000	–	+15
#4A	2015-04-18	16:18	9	120.1632	0.7408	IC	373	+30	5,800	–	+0.5
#5A	2015-04-18	04:41	13	99.6043	−0.3693	IC	342	+30	6,600	18	−0.3
#6F	2015-05-10	21:47	9	−115.9827	7.0164	IC	431	173	9,000	–	+24
#7A	2018-04-14	11:47	11	140.5061	−0.9805	IC	574	+420	8,000	–	−20
#8A	2018-06-16	02:32	9	131.0175	−1.6725	IC	417	+40	6,000	–	+06
#9A	2018-07-19	05:11	10	−79.5522	6.7312	IC	516	+48	6,000	14	+03

From the left: TGFs features (Col. 1–4) ID, data, local time and number of counts observed from space detector. Parent flash characteristics (Col. 5–11): Lat, Lon, type of lightning (intra-cloud/cloud to ground IC/CG flash), Distance from the satellite footprint, peak current and polarity, distance between the flash and the farther sensor on ground and altitude. In Col. 12 Δt is the temporal distance between the TGF event and the GPM observation over the area (negative/positive for previous/consequent crossings in relation to the TGF time).

3. Methods

3.1. Events Selection

The total TGFs database of 1,592 geo-located events (278 detected by AGILE, and 1,314 detected by Fermi), were crossed with GPM orbits. The main selection criteria beyond identification of the storms producing TGFs was to consider a maximum temporal separation between spacecraft observations over a TGF event. A reasonable time range must take into account storm features change (storm cells move rapidly changing their shape, often merge with other storms or split in two or more daughter cells; Houze, 1993).

The choice of the observational time window was based on empirical observations of the average life (growth and decay) on the convective time scale in tropics (∼60 min) and fixed defining a Δt (difference between the TGF time and the time when the GPM satellite passes over the same point on the Earth) of 25 min before and after the event (negative and positive sign indicates an overpass before and after the event, respectively, see Table 1). This time window was selected as a trade-off between the requirement to observe the cloud as close as possible to the time of TGF occurrence, and the need to have a minimum number of cases, since in the case of low-orbit satellites, the chances for quasi-simultaneous observations (here between the TGF detector and the GPM-CO) on the same portion of the earth surface, are very low. The matching of TGF catalogs (Fermi blue dots, AGILE green dots) with GPM-CO orbits provided nine TGFs cases observed by both GMI and DPR, shown in bold in Figure 1 (Fermi black dots, AGILE pink dots. A/F for AGILE/Fermi detection).

In Table 1, for the sample considered, the main TGFs (Col. 1–4) and ENTLN parent flash (Col. 5–11) characteristics are reported. In particular, the TGF is described in terms of date, local time and counts (number of photons observed by the detector). The parent flash is described in terms of geolocation and its distance with respect to the AGILE/Fermi footprint. Furthermore, ENTLN, using a specific stroke classification algorithm and looking at the waveforms data, is able to classify flashes in terms of type (intracloud/cloud to ground IC/CG flash), peak current and polarity, distance between the flash and the farther sensor on ground and altitude. In Col. 12 Δt is the temporal distance between the TGF event and the GPM observation over the area before mentioned.

It is important to underline that many of these TGFs occurred in remote regions, where there are few ENTLN sensors. As such, some of these events were not reported in the ENTLN production system events. However, in all but one case (#2F), enough sensors detected the event to allow for a location to be obtained through a post processing of the raw waveform data. The location was performed using a time-of-arrival

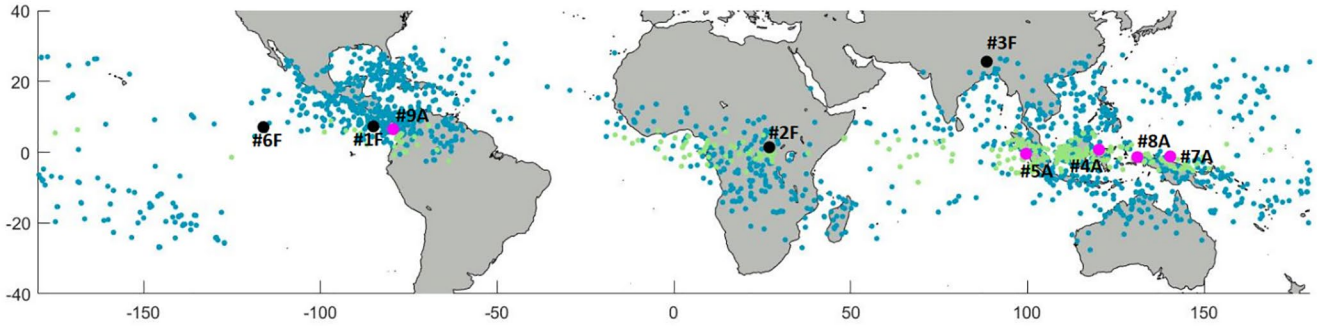

Figure 1. Geographical distribution of the catalogs: Fermi blue dots, AGILE green dots. The nine TGFs-GPM crossed locations in bold (Fermi black dots, AGILE pink dots). Specifics in Table 1. AGILE, Astrorivelatore Gamma a Immagini LEggero; GPM, Global Precipitation Measurement; TGFs, terrestrial gamma ray flashes.

technique and the least squares method built in to Python's Scipy module (https://docs.scipy.org/doc/scipy/reference/generated/scipy.optimize.least_squares.html). For these same events, the peak currents were post processed using the same algorithm used in the ENTLN production system and the classifications were determined by visual inspection.

3.2. Cloud Parameters Estimate

In the two TGF catalogs, each event is associated to the sferic of the related lightning (hereafter referred as "parent flash") starting from the time and position of TGFs. The basic principle to correlate TGFs and lightning makes use of the mechanism under which lightning are able to radiate electromagnetic energy from the Extremely Low Frequency (ELF; 3–30 Hz) to the Medium Frequency (MF; 30 kHz–3 MHz) radio frequency range, commonly known as sferics. In particular, a TGF is assigned to a lightning if its sferic is detected and takes place within a time frame of few hundreds microsecond and 800 km from the satellite footprint (Connauthon et al., 2013).

The parent flash positions are retrieved in the GPM-CO data, selecting the events observed by the DPR in a time interval of 25 min before and after the time of the flash (o TGF) occurrence. In the analysis we'll take into account possible changes in the cloud structures within the time lag between TGF and DPR observations. Then, the TPTs are defined as the Moore 8-neighborhood (Espínola et al., 2015) with near surface radar reflectivity map of the pixel where the parent flash is localized. In this section, we present parameters and indicators we used to classify the TPT according to the characteristics of associated lightning and the cloud structure as revealed by GMI and DPR on board the GPM-CO.

The parameter to classify cloud structures by microwave passive measurements are derived from the GMI product 1C-R that includes radiometrically corrected, geolocated, and intercalibrated TB for all the 13 channels used. During the atmospheric TB estimation, a common problem is due to the land surface contribution. Profiting from the GMI double polarization of window channels, we computed the Polarization Corrected Temperature (PCT; Barrett & Kidd, 1990; Grody, 1984; Kidd, 1998; Spencer et al., 1989; Todd & Bailey, 1995; Toracinta et al., 2002; Weinman & Guetter, 1977). The PCT estimation is the linear combination of TB in H and V polarization that removes much of the effect of varying land surface emissivity. As suggested by Cecil and Chronis (2018), we computed the PCT between 10 and 89 GHz, as:

$$PCT_f = (1 + \Theta_f)TB_{fV} - \Theta_f TB_{fH} \quad (1)$$

where Θ_f is a coefficient that minimizes the effects due to the surface emissivity and TB indicates the TB at frequency f measured for vertical (V) and horizontal (H) polarization (Cecil and Chronis, 2018)

The analysis takes into account different spatial resolutions on each channel (see Table 4) as the measurement corresponding to the TGF could be anywhere within the geolocation uncertainty region.

For the TB at 166 GHz, being sensitive to the upper cloud particles for which no PCT coefficients are available, we considered the absolute difference between the two polarizations as parameter.

For the radar analysis, we used the 2ADPR level 2 product (version 5) geolocated geophysical parameters (Seto & Iguchi, 2015), to investigate the spatial variability of cloud properties and the cloud vertical structure around the TGF by means of different parameters using NS footprint.

According to the double frequency method developed by Colorado State University (Le & Chandrasekar, 2013a, 2013b), the NS footprint is divided into the inner swath (central 125 km), where the dual-frequency (Ku- and Ka-only) data are unified, and the outer swath, where data type is the copy of the corresponding of the Ku-only in a single frequency. The key variable from radar observations is the reflectivity factor Z (dBZ) corrected for total attenuation due to atmospheric gases and precipitating particles (Seto & Iguchi, 2015) to compute several parameters that characterize the cloud (the reflectivity factor, the sixth moment of the cloud particle size distribution, is a measure of the power backscattered by the cloud).

To classify the intensity of convection inside clouds, according to Kumar and Bhat (2016), we considered two types of convective cells. On one hand, the cumulonimbus tower (CbT), which contains a reflectivity factor value of 20 dBZ at 12-km altitude and is at least 9-km deep. On the other hand, the intense convective cloud (ICC), which belongs to the top 5% of the population of the reflectivity factor distribution at a prescribed reference height. In particular, the two reference heights chosen were 3 and 8 km (Kumar & Bhat, 2016) (noting that a convective cell can both qualify as a CbT and an ICC satisfying both definitions).

The physical interpretation of CbT and ICC is as follows: in a cumulonimbus cloud, hydrometeors are transported upwards and once the vertical current is weakened, larger hydrometeors change direction and continue to grow along their descent trajectory. Due to this process the reflectivity assumes the maximum value in the upper troposphere area (E. R. Williams et al., 1989). As hydrometeors descend below the freezing level, Z increases rapidly because of the accretion processes and the transition from ice to liquid phase (Houze, 1993).

These are the reasons why at about 3 and 8 km altitude we expect reflectivity peak (Stith et al., 2002). An important feature of the cloud structure is the distribution of non-precipitating ice particles inside thunderstorms, mainly for two reasons: on one hand, to understand the interactions of photons with the matter they cross, on the other one, to understand what is their link with charge separation in cloud and thus, with lightning. However, Ice Water Content (IWC) in thunderstorms is very difficult to measure with remote instruments: radar reflectivity is proportional to the sixth moment of the particle size distribution, while the IWC is the third moment, and cannot be inferred by reflectivity measurement alone. Nevertheless, different properties of the radar reflectivity vertical structure such as echo top height (Ushio et al., 2001; Williams, 1985) or maximum radar reflectivity at different altitudes (Cecil et al., 2005; Pessi & Businger, 2009; Zipser & Lutz, 1994) have been related to the flash rate (FR).

Several studies in the past have estimated the Z-IWC relationship. Petersen and Rutledge (2001) combine both TRMM PR and LIS data to examine vertical structures and ice water contents, finding a largest systematic variability in precipitation vertical structure observed between all of the locations examined occurred above the freezing level.

Rutledge et al. (2000) used data from the TRMM-LBA field campaign emphasizing the kinematic and microphysical characteristics observed in two specific convective systems utilizing ground based dual-Doppler and S-band polarimetric radar data. Since the lightning production inside cloud is strongly related to the presence of graupel (frozen particles with density lower than hailstone, characterized by Z values greater than ~30 dBZ above the freezing level (Jayaratne et al., 1983; Lopez & Aubagnac, 1997; Saunders et al., 1991; Takahashi, 1978), we here consider the graupel extension (km) as the maximum altitude with $Z > 30$ dBZ above the freezing level (Graupel Top in Table 2). Other key variables extracted from DPR products are: Surface type, height storm top, and flag anvil (a new item added in version 5 of the GPM algorithm to better classify storm shape). The possible values of flag Anvil are as follows: Flag Anvil = 1: Anvil is detected, flag Anvil = 0: Anvil is not detected (including the case of data missing; Iguchi et al., 2002).

As mentioned above, from the GMI observations we took advantage of the availability of dual polarization channels from 10 to 166 GHz, and computed the Polarization Corrected Temperature (PCT) calculation in the channels between 10 and 89 GHz from Cecil and Chronis (2018) (Col. 15–18). In the case of the TB at

Table 2
DPR Cloud Features

ID	Surf.	Cloud top (km)	Flag Anvil	Z_{max} (dBz)	ICC3 (dBZ)	ICC8 (dBZ)	CbT	Gr. Top (km)
#1F	O	15.7	0	54.4	54.4	39.3	1	0.1
#2F	L	16.0	0	53.0	53.0	39.7	1	2.2
#3F	L	15.9	1	60.3	54.6	43.3	1	7.0
#4A	C	15.2	0	44.6	42.2	32.2	1	7.2
#5A	C	16.0	0	53.0	53.0	39.7	1	6.4
#6F	O	15.8	1	49.6	49.6	29.5	1	4.2
#7A	O	14.5	0	51.8	51.8	39.4	1	5.6
#8A	O	16.7	1	58.3	58.3	44.3	1	5.4
#9A	C	16.5	0	56.3	56.3	39.8	1	7.6

From GPM products: Surface type (O/C/L for Ocean/Coast/Land), Cloud top height (km), Flag Anvil, Maximum value for the reflectivity factor (corrected for non-precipitating particles). Derived variables: ICC3-8 reflectivity factor values for 3-8 km altitude, respectively, Flag Cloud tower, Graupel top in its vertical extension.

166 GHz, for which no PCT coefficients are available, we considered the absolute difference between the two polarizations as parameter.

Tables 2 and 3 summarize the characteristics of the clouds related to all the TGFs events considered, derived by the DPR and GMI instruments.

3.3. Comparison With Statistics

3.3.1. DPR

Kumar and Bhat (2016) develop a model to classify the intensity of the convective clouds based on the vertical profiles of radar reflectivity. Their model is based on the analysis of 10 years of reflectivity data as derived from the TRMM PR measurements. They considered the cloud parameters ICC3 and ICC8 (above described) derived from the vertical profiles of reflectivity measured in 18 locations distributed across the tropics and two locations in the subtropics.

Table 5 shows $ICC3_{ref}$ and $ICC8_{ref}$ thresholds in different areas found by Kumar and Bhat (2016) to label the cloud as intense convective, the ICC3 and ICC8 calculated for the nine case studies considered in this work, while ΔICC3 and ΔICC8 represents the respective differences derived from the comparison between them.

It was observed that ICC8 and ICC3 thresholds are in the 28–35 and 40–43 dBZ ranges, with variance values σ^2 of 0.5 and 1.8 units, respectively. For ICC3, in all nine cases, we have $\Delta ICC3 \gg \sigma$, with a maximum difference with respect to the reference value of 17.3 dBZ (case #8A). ICC8 reflects this trend too, showing only 2/9 cases (#4A and #6F) with ICC values below the respective reference values. On the other hand, a CbT is defined as a fixed Z threshold value of 20 dBZ at 12-km altitude, and its base is located below the 3-km altitude (Kumar & Bhat, 2016). For our case studies 100% present these characteristics.

3.3.2. GMI

On the other hand, the GMI measurements are investigated in order to classify events in a more general convection framework. The approach is based on the study from Cecil and Chronis (2018).

In their work, hydrometeor types are derived from dual polarization radar hydrometeor identifications in the GPM Validation Network database of matchups between the GMI and dozens of ground radars mostly in the U.S., and ranked in a hierarchy as: hail or large drops, high-density graupel, low-density graupel, snow, ice crystals, rain, and drizzle. For any given GMI footprint, the brightness polarization corrected temperatures (PCT) are assigned to the highest ranking hydrometeor category anywhere in that footprint, with ranking based on the hierarchy above. Figure 2 shows for 89 GHz PCT the probability of a given hydrometeor type being present over the sample considered, showing a likelihood of hail/graupel exceeding 80% in 7/9 events. The exceptions (#1F and #6F) have a large time difference between TGF occurrence and observation: during 11 and 24 min (respectively) the cloud could have moved and/or changed significantly its structure.

We carried out a detailed analysis on the nine TPT and we will present the results related to a representative event in which the cloud develops and was observed entirely in the radar field of view. Moreover, this case represents the event with the highest TGF intensity (number of counts measured by the detector). It was observed by Fermi and occurred on September 11, 2014 at 09:04 a.m. local time over Bangladesh (case #3F).

4. Case Study: Fermi TGF on 2014/09/11 Over Bangladesh

On September 11, 2014, at 03:04 UT (09:04 a.m. local time), Fermi GBM detected a TGF over Bangladesh. The event has, in the corresponding catalog, WWLLN association. The ENTLN post processed location was 9.2 km from the WWLLN detection, indicating good agreement within errors (see Figure 3a).

Table 3
GMI Cloud Features

ID	PCT10 (K)	PCT19 (K)	PCT37 (K)	PCT89 (K)	166 V-H (K)
#1F	286	276	256	145	0.7
#2F	281	271	227	136	4.0
#3F	293	270	225	117	2.5
#4A	290	291	284	151	13.7
#5A	283	278	220	118	1.4
#6F	281	282	276	276	0.2
#7A	291	288	259	145	3.0
#8A	293	289	282	188	11.3
#9A	284	276	246	133	4.3

PCT values (K) for channels 10, 19, 37 and 89 GHz from (Cecil & Chronis, 2018). For channel 166 GHz the absolute difference between vertical and horizontal polarization.

The ENTLN system can discriminate IC from CG strokes, locate, and when possible, estimate the height of IC emission. The farther sensor that measured the event is distant 5,000 km, recording a very intense positive IC flash with a peak current of 86 kA. Figure 3c shows the waveform from this event detected by the closest sensor. There are two pulses occurring a few milliseconds apart, which are illustrated in separate panels to allow for better temporal detail. This sensor is only 166 km away from the parent flash, relatively close. Considering that there is no indication of a return stroke signature, which would manifest as a very fast rising edge, typically lasting around 1 microsecond (Rakov & Uman, 2003). Therefore, we can be confident that this event was in fact an IC. The number of counts measured by Fermi GBM is 20.

We first analyze the temporal evolution of the CG and IC combined registered strokes using the ENTLN data. To determine the storm phase in which the TGF is generated, ENTLN lightning data in proximity of TGF are examined in terms of flash rate (FR) variation, over 1 h time window and 40 km space ranges centered to the TGF time and location.

The timeline of the activity is as follow (Figure 3b): the cloud starts to produce lightning at 02:40 local time, 18 min before the TGF emission. The flash rate increases reaching its maximum during the TGF event at 03:04 local time, dropping down of a factor of 5 in the following 10 min. The relation between the TGF occurrence and the flash rate trend is consistent with what shown in Tiberia et al. (2019) and Ursi (2019), highlighting that a TGF often occurs during the most active lightning phase of the storm.

GPM-CO captures the event 15 min after that Fermi GBM detected the TGF from space. Here the entire convective system is captured by the DPR inner swath. Different features of the storms can be extracted from TBs measured at different frequencies. We first focus on quantities derived from high frequencies on GMI (e.g., 89 and 166 GHz), that can be directly related to the ice hydrometeor presence on cloud top. The GMI dual polarization channels at 166 GHz makes it possible to observe the preferential orientation of ice crystals in the cloud top layers (Defer et al., 2014).

The TGF emission area is identified by V-H value of 2.5 K (see Table 3) very close to 0 indicating that there is no preferential direction of particles, denoting the presence of randomly oriented ice particles, which is usually interpreted as strong updraft currents (Prigent et al., 2005).

To analyze events from a more quantitative point of view, vertical cross sections of the storm are rendered in a parallel and perpendicular directions with respect to the satellite flight direction (along-track [AT] and cross-track [CT] directions, respectively), shown as black solid lines on the near surface level (NSL) reflectivity map (Figures 4b and 4c).

The two vertical cross sections are shown in Figures 4b and 4c where the columnar cloud structure is rendered in color shades and the TGF location is indicated (black vertical line). Corresponding TB (in vertical polarization, V-pol) profiles are plotted in the upper part of the panel (scale on the right *y*-axis). Moreover, the horizontal bar on the top of the plot indicates the type of surface (blue for water and brown for land).

As can be seen from the NSL reflectivity map (Figure 4a), the TGF took place near the core area of the cloud and well centered in the DPR swath, where the double frequency data were available. The maximum altitude was about 16 km with maximum reflectivity values reached up in the core was about 60 dBZ.

CT and AT cross sections show a well-defined structure, including the anvil and the main deep convective area. Moreover, Figure 4c shows the presence of a stratiform area at the edge of the main core, highlighted by the presence of a bright band.

With the aim to evaluate the presence and the vertical distribution of graupel particles ($Z > 30$ dBZ over the freezing level – blue line), Figure 5 maps vertical profiles of Z factor for the pixel where the TGF is geolocated (black curve), as well as for 3×3 neighborhood pixels around it (magenta curves).

Table 4
Spatial Resolution (km) for GMI Channels From 10 to 89 GHz and Coefficients for PCT Formulas (Cecil & Chronis, 2018)

$f_{(GHz)}$	Res.$_{(km)}$	Θ_f
10	32 × 19	1.50
19	18 × 11	1.40
37	15 × 9	1.15
89	7 × 4	0.70

Figure 5 shows, for this event, the presence of a very deep layer with likely presence of graupel, reaching an altitude of 7 km.

5. Discussion and Conclusions

At the light of the state-of-the-art and knowledge gaps in the understanding of correlation between TGFs and meteorological phenomena, the present study aimed to explore thunderclouds producing TGFs, monitoring on ground lightning rate combined with spaceborne sensors observations for cloud characterization.

The present study takes advantage of the availability of satellite radar data to perform analysis of the vertical structure of TGFs producing thunderclouds from a new perspective, by exploiting storms observed simultaneously by a suite of sensors onboard the GPM-CO. Moreover, ENTLN lightning network, with the possibility of performing several analyzes to the TGFs parent flash are considered.

A total of 1,592 TGFs from the 3rd AGILE TGF catalog and the Fermi catalog were crossed with GPM orbits, finding a subsample of nine events inside both the DPR and GMI swath within 25 min.

Table 3 shows that the events are mostly detected over coast and ocean, rather than land. Despite the limited sample and the applied selection criteria, this is consistent with the general trend reported for TGFs detected by RHESSI, Fermi and AGILE, which are shown to cluster over coastal regions (Albrechtsen et al., 2019; Lindanger et al., 2020; Roberts et al., 2018). In particular, Lindanger et al. (2020) showed that the geographical distribution of TGFs does not match exactly the geographical distribution of lightning detected by WWLLN, TGFs occurring relatively more often 150 km from the coastline. This observation is still currently matter of debate, possible explanations can be linked to the extended charging period prior to TGFs (Larkey et al., 2019), and the role of CAPE and aerosol concentration suggested as responsible for the depletion of the TGF to lightning ratio in Central Africa (Fabró et al., 2019).

Looking at Table 1, spherics of the parent flashes to these events were detected by electric field sensors 6,000–9,000 km away, indicating that they are very powerful. Furthermore, visual inspection of the ENTLN waveforms indicate that all of these events are high amplitude IC flashes. This confirm previous results that found an association of TGF events to powerful positive IC flashes (Shao et al., 2010). In only three out of nine cases, the altitude of the IC flash associated to the TGFs can be estimated, and it is found to be in the upper cloud layers. GPM measurements allow for the delineation of cloud structure in a three-dimensional view, with high spatial resolution.

Observations of cloud topography and clouds vertical development, show that not all cases are isolated thunderstorms but areas often experience multiple convective cells with high cloud top height. The

Table 5
Reflectivity Thresholds for ICC3 and ICC8 Cells for Selected Areas for Comparison (Adapted From Kumar & Bhat, 2016) and Reflectivity Values for Our Events

No.	Area/Region	ICC3$_{ref}$ (dBZ)	ICC8$_{ref}$ (dBZ)	ICC3 (dBZ)	ICC8 (dBZ)	ΔICC3 (dBZ)	ΔICC8 (dBZ)	CbT
#1F	Equatorial South America (LAM)	42.5	34.0	54.4	39.3	+11.9	+5.3	√
#2F	Equatorial Africa (AF)	43.0	35.0	53.0	39.7	+10.0	+4.7	√
#3F	Indo-Gangetic Plain (IGP)	42.0	31.0	54.6	43.3	+12.6	+12.3	√
#4A	Maritime Continent (MCw)	41.0	33.5	42.2	32.2	+1.2	−1.3	√
#5A	Indian Ocean east (IOEs)	41.0	28.5	53.0	39.7	+12.0	+11.2	√
#6F	Equatorial South America (LAM)	42.5	34.0	49.6	29.5	+5.4	−4.5	√
#7A	Maritime Continent (MCw)	41.0	33.5	51.8	39.4	+10.8	+4.9	√
#8A	Maritime Continent (MCw)	41.0	33.5	58.3	44.3	+17.3	+10.8	√
#9A	Equatorial South America (LAM)	42.5	34.0	56.3	39.8	+13.8	+5.8	√

ΔICC3 and ΔICC8 represent differences derived from the comparison in the same area.

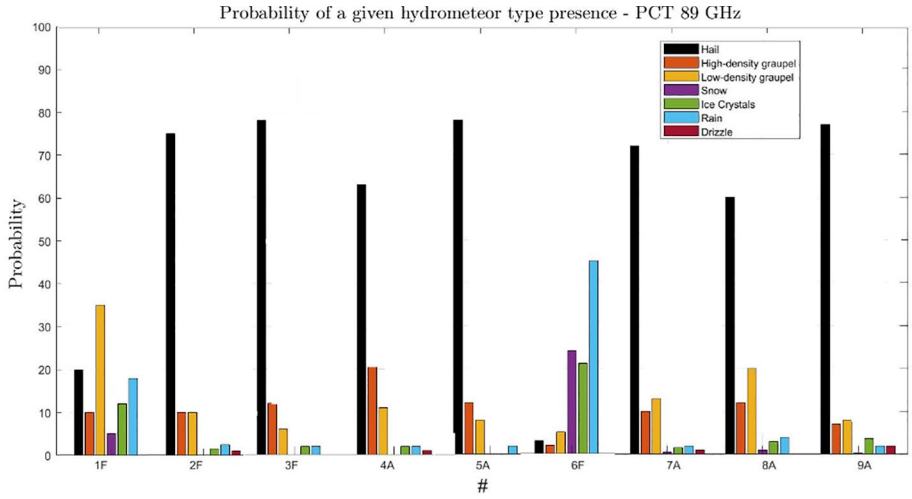

Figure 2. The probability of a given hydrometeor type being present for channel 89 GHz, for individual cases.

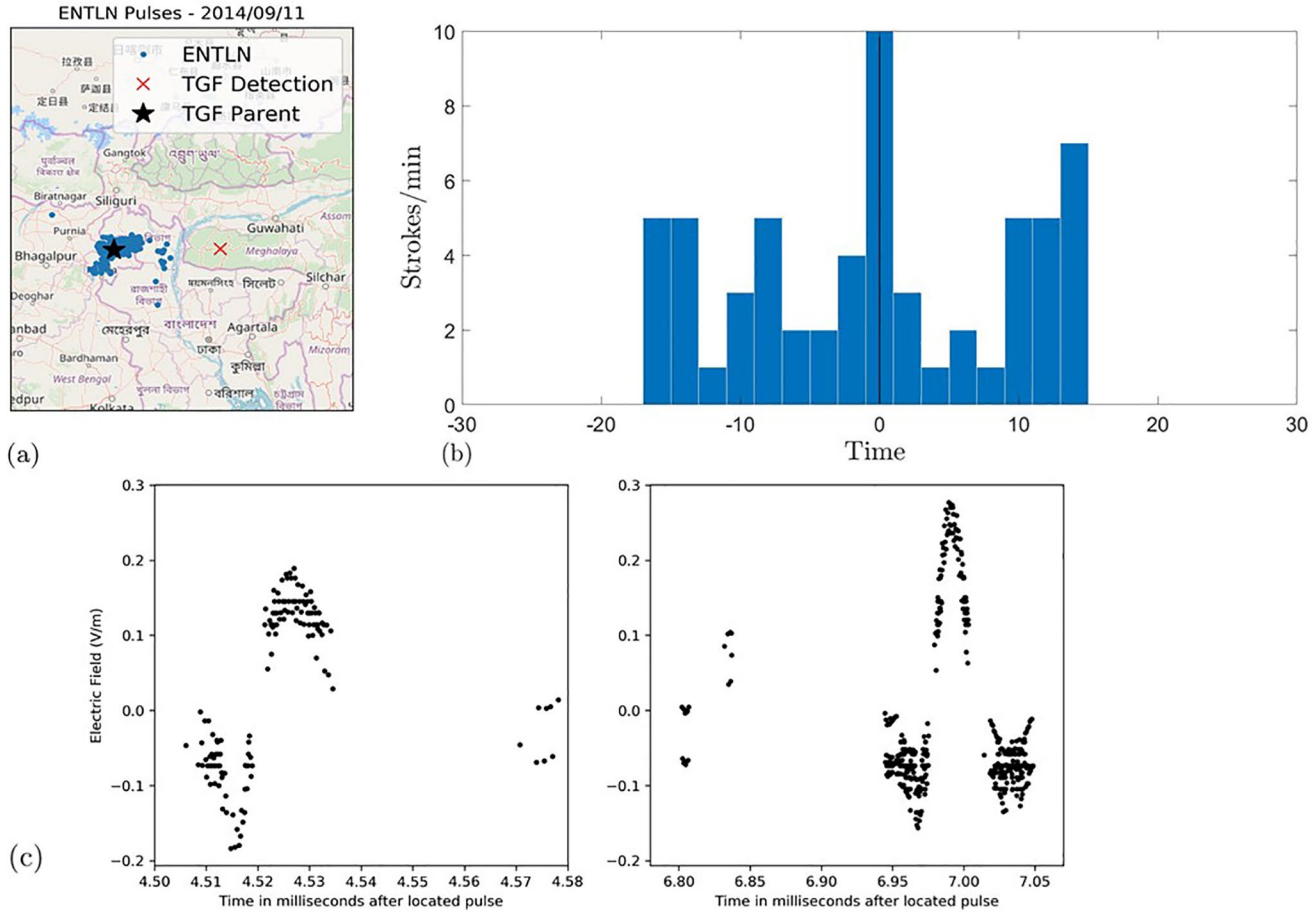

Figure 3. Case #3F (a): ENTLN Lightning flash map around the TGF satellite detection (red cross). The black star represents the associated parent flash. Blue dots all lightning detected. (b): FR histogram in a 40 km radius area around the event Bin size 2 min. TGF in 0 (c) Parent flash waveform. ENTLN, Earth Networks Total Lightning Network; TGF, terrestrial gamma ray flash.

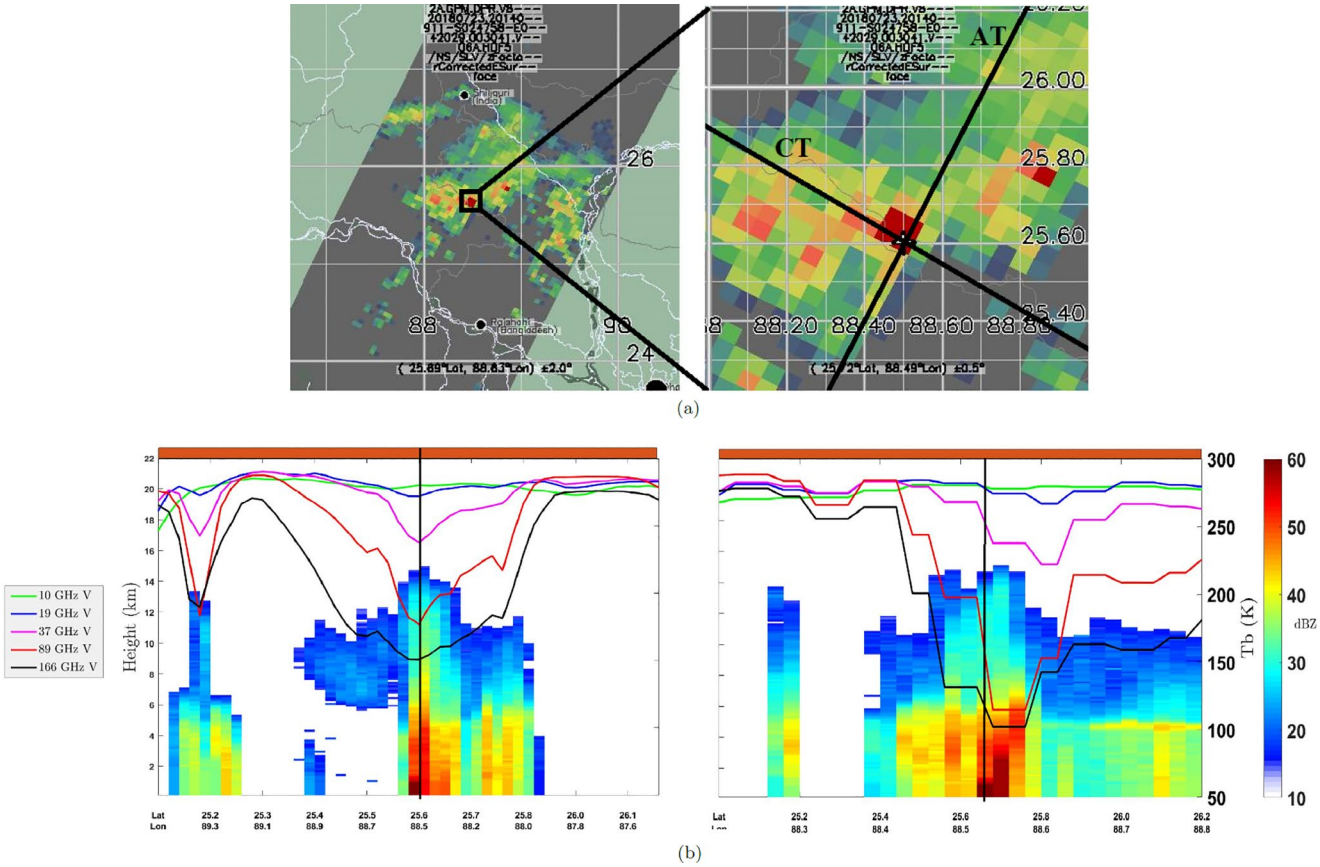

Figure 4. Case #3F (a): NSL reflectivity factor map. The black lines are the CT and AT cutting directions centered on the TGF location. (b), (c): DPR reflectivity at CT and AT sections. The profiles of the corresponding TB (V pol) are plotted in the upper part of the panel (scale on the right axis). The bar at the top indicates the type of the surface (blue for water/brown for land). TGF source location is the black line. AT, along-track; CT, cross-track; DPR, Dual-frequency Precipitation Radar; NSL, near surface level; TB, Brightness Temperatures; TGF, terrestrial gamma ray flash.

maximum storm height values for every TGF in the sample are below 16.7 km, whereas the minimum can range from ~14.5–15.2 km. Although the statistics are limited, we note that the available lightning altitude estimate and the observed cloud top altitudes are not compatible with TGFs being produced at low altitudes,

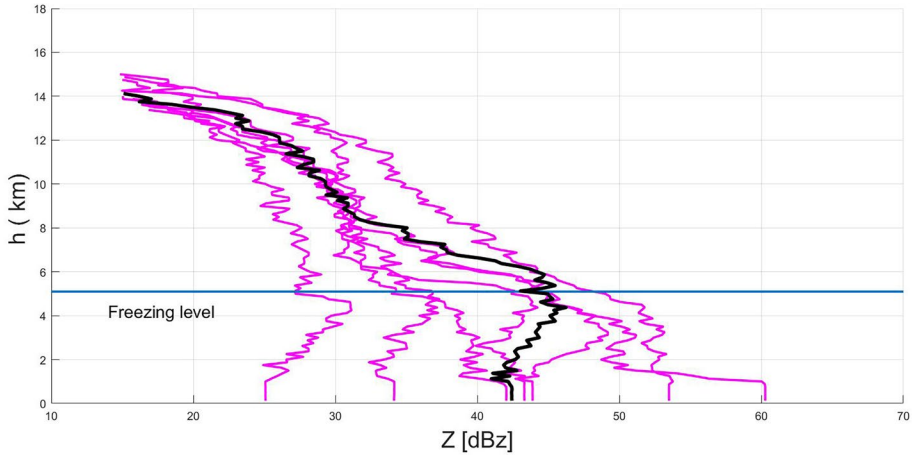

Figure 5. Vertical profiles of reflectivity factor values for pixel corresponding to the TGF location (black curve) and for the 3 × 3 neighborhood pixels around (magenta curves). The blue line represents the freezing level. TGF, terrestrial gamma ray flash.

supporting the conclusions of Smith et al. (2016) that TGFs produced at low altitude can account only for a very small fraction of the total number of TGFs. Despite it is well known that a higher flash density is found over land, only two out of nine TPT occurred inland. In fact, this is in agreement with previous analysis showing that coastal (or ocean) thunderstorms are more prone to produce TGF (Albrechtsen et al., 2019; Lindanger et al., 2020; Roberts et al., 2018).

The radar reflectivity profile, and its variability within the cloud volume, are used to investigate vertical cloud structure by means of space-borne radar. In all the case studies we notice the presence of an intense updraft current in which the high reflectivity columns reach at least 7 km in height with Z above 30 dBz, indicating the presence of ice well up in the cloud structure, with likely distribution of graupel and hail. TGFs locations are very close, or coincident, to these high Z columns, where reflectivity exceeds 50 dBz.

In order to evaluate our findings with respect to other studies, we compare reflectivity features with respect to literature. Features of convective clouds are extracted in line with ICC3, ICC8, and CbT definitions by Kumar and Bhat (2016), and compared with regional values across tropics. We find very intense values with respect to reflectivity thresholds reference over tropics. The ICC parameter, calculated for two reference heights (3 and 8 km), showed exceeding values for 100% of cases up to 17.3 dBZ for 3 km height and for 77% of cases up to 12.3 dBZ for 8 km. On the other hand, 100% of cases present a CbT.

Most of these cloud structures present common and coherent features, contain at least one profile reaching 14 km a.s.l. or more, while the reflectivity reaches very high values (in the range 50–60 dBz) for most of the profiles. Above the FL, all storms show rather thick layers with reflectivity exceeding 30 dBz, indicating the presence of graupel.

However, graupel extension shows high variability in the range of 0.1–7.6 km over the freezing level.

This variability could depend on the spatial resolution of the measure: graupel distribution is not calculated on the entire convective system, but on a neighborhood of 3 × 3 pixels (15 × 15 km) around the TGFs location. In this perspective, considering the Δt between the lightning occurrence and the GPM observation, it must be taken into account that in this time interval the cloud has moved and probably, the observation in a narrow spatial range may be changed.

In a global vision of the entire clouds involved, parameters consistently show intense clouds with the presence of convective towers in all cases.

The analysis of the TB cross sections, high frequencies (89 and 166 GHz) show strong depression in correspondence to the TGFs location, indicating the presence of a thick ice layer. PCT for lower frequencies, more sensitive to the emission of radiation from raindrops, shows a moderate increase with respect to cold ocean, in correspondence to the main updraft. At lower frequencies the signal is less evident, and very small perturbation (few K) is shown in the TB profiles across the TGFs position. This could be due to the small scale of the most intense rain shaft, since lower frequencies have coarser resolution, or to the limited thickness of rain layer.

All thunderstorms show a very strong depression of PCT89, with the exception of case #6F. This indicates a strong scattering signal by a thick ice layer in the upper cloud layers. For the lower frequencies (especially 10 and 19 GHz), the values are closer to each other and to the expected thermodynamic temperature of the observed objects (clouds). Because the low density ice particles in the upper cloud layers have higher scattering efficiency at the higher frequency (Defer et al., 2014; Marra et al., 2017), TB values can be related to the orientation of the ice hydrometeors in the cloud (Defer et al., 2014; Spencer et al., 1989).

In that way, using the dual polarization feature of the GMI radiometer, it is possible to calculate the V-H signal and thus the orientation of non-spherical ice crystals in the area around the TGFs emission. Here the signal always returns positive values, from 0.2 K up to 13.7 K indicating a complex structure and different hydrometeor characteristics in the upper cloud layers: randomly oriented ice particles (V-H values around 0) brought to the upper levels by the strong updraft in the convective core, and vertically oriented ice particles. An empirical use of PCT was used to characterize the analyzed storms in terms of hydrometeor types, confirming in 7/9 cases a high likelihood of hail/graupel presence.

Finally, in this observational analysis, both active and passive microwave views of the considered thunderstorms agree in describing TGFs producing clouds as intense thunderstorms, with significant vertical development and ice content. These results seems to be in contrast with examinations over 24 TGF-producing storms conducted by Chronis et al. (2016), where a variety of convective strengths with no distinguishing characteristics were found.

We note that both studies (Chronis et al., 2016, and the present one) use WWLLN and ENTLN for geolocating TGFs. However, Chronis et al. (2016) limit the sample to events over the Continental United States, where the WWLLN detection efficiency is larger, see Figure 4 in Hutchins et al. (2012). The sample presented in this work is global, extended worldwide to regions with relatively low lightning detection efficiency, therefore more prone to a bias toward large-scale convective systems with extensive lightning activity, more easily detectable. We regard this as a viable explanation to the discrepancies between our work and Chronis et al. (2016). We point out that this is an unavoidable bias affecting every global TGF sample requiring lightning association, which is in turn a mandatory requirement if a location of the source with accuracy below tens of km is needed. We note that this bias affects also other studies on the meteorological characteristics of TGF-producing thunderstorms, such as Smith et al. (2010), Splitt et al. (2010), and Ursi (2019). Here we summarize the main results of the study:

1. We present a subset of nine geolocated TGFs with concurrent (within 25 min) observations from passive (radiometers) and active (radar) sensors onboard the GPM core satellite
2. All events are associated to powerful positive intra-cloud (+IC) lightning flashes;
3. In all cases the TGFs are produced within intense clouds with the presence of convective towers
4. All TGF locations are very close or coincident with high reflectivity regions, indicating the presence of ice, well up in the cloud structure
5. There is evidence for a complex structure of hydrometeors with different characteristics in the upper cloud layers
6. An empirical classification of the hydrometeor type points to the presence of graupel and hail in seven cases out of nine

Data Availability Statement

The data for the TGF sample presented in this work are publicly available at the ASI Space Science Data Center (SSDC) website (https://www.ssdc.asi.it/mcal3tgfcat) for the AGILE data set and NASA GBM Instrument Operations Center (GIOC) website (https://fermi.gsfc.nasa.gov/ssc/data/access/gbm/tgf) for the Fermi ones. The GPM data products are available to the science community from the Precipitation Processing System (PPS) website (pps.gsfc.nasa.gov).

Acknowledgments
This study was supported by the National Research Council (CNR) of Italy and by the Research Council of Norway under contracts 208028/F50 and 223252/F50 (CoE). The authors wish to thank the World Wide Lightning Location Network (http://wwlln.net), a collaboration among over 50 universities and institutions, for providing the lightning location data used in this study and Dr. Isabella Riva, Dr. Florenci Ray Benadero and Dr. Steve Prinzivalli for providing access to the Earth Networks Total Lightning Network (https://earthnetworks.com) lightning data.

References

Albrechtsen, K. H., Østgaard, N., Berge, N., & Gjesteland, T. (2019). Observationally weak TGFs in the RHESSI data. *Journal of Geophysical Research: Atmosphere*, *124*(1), 287–298. https://doi.org/10.1029/2018JD029272

Barnes, D. E., Splitt, M. E., Dwyer, J. R., Lazarus, S., Smith, D. M., & Rassoul, H. K. (2015). A study of thunderstorm microphysical properties and lightning flash counts associated with terrestrial gamma-ray flashes. *Journal of Geophysical Research: Atmospheres*, *120*, 3453–3464. https://doi.org/10.1002/2014JD021495

Barrett, E. C., & Kidd, C. (1990). Rainfall monitoring by the SSM/I in the midlatitudes. In *Fifth Conference Satellite Meteorology Oceanography* (pp. 210–214). American Meteorological Society.

Briggs, M. S., Xiong, S., Connaughton, V., Tierney, D., Fitzpatrick, G., Foley, S., et al. (2013). Terrestrial gamma-ray flashes in the Fermi Era: Improved observations and analysis methods. *Journal of Geophysical Research: Space Physics*, *118*(6), 3805–3830. https://doi.org/10.1002/jgra.50205

Bui, V., Chang, L.-C., & Heckman, S. (2015). A performance study of Earth Networks Total Lighting Network (ENTLN) and Worldwide Lightning Location Network (WWLLN). In *2015 International Conference on Computational Science and Computational Intelligence (CSCI)* (pp. 386–391). https://doi.org/10.1109/CSCI.2015.120

Cecil, D. J., & Chronis, T. (2018). Polarization-Corrected Temperatures for 10-, 19-, 37-, and 89-GHz Passive Microwave Frequencies. *Journal of Applied Meteorology and Climatology*, *57*(10), 2249–2265. https://doi.org/10.1175/JAMC-D-18-0022.1

Cecil, D. J., Goodman, S. J., Boccippio, D. J., Zipser, E. J., & Nesbitt, S. W. (2005). Three years of TRMM precipitation features. Part I: Radar, radiometric, and lightning characteristics. *Monthly Weather Review*, *133*, 543–566. https://doi.org/10.1175/mwr-2876.1

Christian, H., Blakeslee, R., Goodman, S., Mach, D., Stewart, M., Buechler, D., et al. (1999). The lightning imaging sensor. In *NASA conference publication*. NASA.

Chronis, T., Briggs, M. S., Priftis, G., Connaughton, V., Brundell, J., Holzworth, R., et al. (2016). Characteristics of thunderstorms that produce terrestrial gamma ray flashes. *Bulletin of the American Meteorological Society*, *97*, 639–653. https://doi.org/10.1175/BAMS-D-14-00239.1

Connaughton, V., Briggs, M. S., Xiong, S., Dwyer, J. R., Hutchins, M. L., Grove, J. E., et al. (2013). Radio signals from electron beams in terrestrial gamma ray flashes. *Journal of Geophysical Research: Space Physics*, *118*(5), 2313–2320. https://doi.org/10.1029/2012JA018288

D'Adderio, L. P., Porcú, F., Panegrossi, G., Marra, A. C., Sanò, P., & Dietrich, S. (2019). Comparison of the GPM DPR single- and double-frequency products over the Mediterranean Area. In *IEEE Transactions on Geoscience and Remote Sensing*. *57*(12), 9724–9739). https://doi.org/10.1109/tgrs.2019.2928871

D'Adderio, L. P., Vulpiani, G., Porcú, F., Tokay, A., & Meneghini, R. (2018). Comparison of GPM core observatory and ground-based radar retrieval of mass-weighted mean raindrop diameter at midlatitude. *Journal of Hydrometeorology*, *19*(10), 1583–1598. https://doi.org/10.1175/JHM-D-18-0002.1

Defer, E., Galligani, V. S., Prigent, C., & Jimenez, C. (2014). First observations of polarized scattering over ice clouds at close-to-millimeter wavelengths (157 GHz) with MADRAS on board the Megha-Tropiques mission. *Journal of Geophysical Research: Atmospheres*, *119*(21), 12,301–12,316. https://doi.org/10.1002/2014JD022353

Dwyer, J. R., & Smith, D. M. (2005). A comparison between Monte Carlo simulations of runaway breakdown and terrestrial gamma-ray flash observations. *Geophysical Research Letters*, *32*, L22804. https://doi.org/10.1029/2005GL023848

Espínola, M., Piedra-Fernandez, J. A., Ayala, R., Iribarne, L., & Wang, J. Z. (2015). Contextual and hierarchical classification of satellite images based on cellular automata. In *IEEE Transactions on Geoscience and Remote Sensing* (Vol. 53(2), pp. 795–809). https://doi.org/10.1109/tgrs.2014.2328634

Fabró, F., Montanyà, J., Velde, O. A., Pineda, N., & Williams, E. R. (2019). On the TGF/lightning ratio asymmetry. *Journal of Geophysical Research: Atmospheres*, *124*, 6518–6531. https://doi.org/10.1029/2018JD030075

Fishman, G. J., Bhat, P. N., Mallozzi, R., Horack, J. M., Koshut, T., Kouveliotou, C., et al. (1994). Discovery of intense gamma-ray flashes of atmospheric origin. *Science*, *264*, 1313–1316. https://doi.org/10.1126/science.264.5163.1313

Fuschino, F., Marisaldi, M., Labanti, C., Barbiellini, G., Del Monte, E., Bulgarelli, A., et al. (2011). High spatial resolution correlation of AGILE TGFs and global lightning activity above the equatorial belt. *Geophysical Research Letters*, *38*(14), L14806. https://doi.org/10.1029/2011GL047817

Grody, N. C. (1984). Precipitation monitoring over land from satellites by microwave radiometry. In *Proceedings of the IGARSS'84 Symposium, Strasbourg, 27–30 August 1984*.

Hou, A. Y., Kakar, R. K., Neeck, S., Azarbarzin, A. A., Kummerow, C. D., Kojima, M., et al. (2014). The global precipitation measurement mission. *Bulletin of the American Meteorological Society*, *95*, 701–722. https://doi.org/10.1175/BAMS-D-13-00164.1

Houze, R. A., Jr. (1993). *Cloud Dynamics* (pp. 573). Academic Press.

Hutchins, M. L., Holzworth, R. H., Brundell, J. B., & Rodger, C. J. (2012). Relative detection efficiency of the world wide lightning location network. *Radio Science*, *47*(6). https://doi.org/10.1029/2012RS005049.rS6005

Iguchi, T., Oki, R., Smith, E., & Furuhama, Y. (2002). Global precipitation measurement program and the development of dual-frequency precipitation radar. *Communications Research Laboratory Journal*, *49*, 37–46.

Jayaratne, E. R., Saunders, C. P. R., & Hallett, J. (1983). Laboratory studies of the charging of soft-hail during ice crystal interactions. *Quarterly Journal of the Royal Meteorological Society*, *109*(461), 609–630. https://doi.org/10.1002/qj.49710946111

Kidd, C. (1998). On rainfall retrieval using polarization-corrected temperatures. *International Journal of Remote Sensing*, *19*, 981–996. https://doi.org/10.1080/014311698215829

Kumar, S., & Bhat, G. S. (2016). Vertical profiles of radar reflectivity factor in intense convective clouds in the tropics. *Journal of Applied Meteorology and Climatology*, *55*, 1277–1286. https://doi.org/10.1175/JAMC-D-15-0110.1

Labanti, C., Marisaldi, M., Fuschino, F., Galli, M., Argan, A., Bulgarelli, A., et al. (2009). Design and construction of the Mini-Calorimeter of the AGILE satellite. *Nuclear Instruments and Methods in Physics Research Section A: Accelerators, Spectrometers, Detectors and Associated Equipment*, *598*, 470–479. https://doi.org/10.1016/j.nima.2008.09.021

Larkey, R. K., Sample, J. G., Smith, D. M., Briggs, M. S., Lapierre, J. L., & Holzworth, R. H. (2019). Evidence for extended charging periods prior to terrestrial gamma ray flashes. *Geophysical Research Letters*, *46*(17–18), 10619–10626. https://doi.org/10.1029/2019gl083827

Le, M., & Chandrasekar, V. (2013a). Hydrometeor profile characterization method for dual-frequency precipitation radar onboard the GPM. *IEEE Transactions on Geoscience and Remote Sensing*, *51*, 3648–3658. https://doi.org/10.1109/TGRS.2012.2224352

Le, M., & Chandrasekar, V. (2013b). Precipitation type classification method for dual-frequency precipitation radar (DPR) onboard the GPM. *IEEE Transactions on Geoscience and Remote Sensing*, *51*, 1784–1790. https://doi.org/10.1109/TGRS.2012.2205698

Lindanger, A., Marisaldi, M., Maiorana, C., Sarria, D., Albrechtsen, K., Østgaard, N., et al. (2020). The 3rd agile terrestrial gamma ray flash catalog. Part I: Association to lightning sferics. *Journal of Geophysical Research: Atmospheres*, *125*, e2019JD031985. https://doi.org/10.1029/2019JD031985

Liu, C., & Heckman, S. (2011). The application of total lightning detection and cell tracking for severe weather prediction. In *91st American Meteorological Society Annual Meeting* (pp. 1–10).

López, R. E., & Aubagnac, J.-P. (1997). The lightning activity of a hailstorm as a function of changes in its microphysical characteristics inferred from polarimetric radar observations. *Journal of Geophysical Research*, *102*(D14), 16799–16813. https://doi.org/10.1029/97jd00645

Maiorana, C., Marisaldi, M., Lindanger, A., Østgaard, N., Ursi, A., Sarria, D., et al. (2020). The 3rd AGILE terrestrial gamma-ray flashes catalog. Part II: Optimized selection criteria and characteristics of the new sample. *Journal of Geophysical Research: Atmospheres*, *125*(11), e2019JD031986. https://doi.org/10.1029/2019JD031986

Mallick, S., Rakov, V. A., Hill, J. D., Ngin, T., Gamerota, W. R., Pilkey, J. T., et al. (2015). Performance characteristics of the ENTLN evaluated using rocket-triggered lightning data. *Electric Power Systems Research*, *118*, 15–28. https://doi.org/10.1016/j.epsr.2014.06.007

Marchand, M., Hilburn, K., & Miller, S. D. (2019). Geostationary lightning mapper and earth networks lightning detection over the contiguous united states and dependence on flash characteristics. *Journal of Geophysical Research: Atmospheres*, *124*(21), 11552–11567. https://doi.org/10.1029/2019jd031039

Marisaldi, M., Fuschino, F., Labanti, C., Galli, M., Longo, F., Del Monte, E., et al. (2010). Detection of terrestrial gamma ray flashes up to 40 MeV by the AGILE satellite. *Journal of Geophysical Research*, *115*, A00E13. https://doi.org/10.1029/2009JA014502

Marisaldi, M., Fuschino, F., Tavani, M., Dietrich, S., Price, C., Galli, M., et al. (2014). Properties of terrestrial gamma ray flashes detected by AGILE MCAL below 30 MeV. *Journal of Geophysical Research: Space Physics*, *119*(2), 1337–1355. https://doi.org/10.1002/2013JA019301

Marra, A. C., Porcù, F., Baldini, L., Petracca, M., Casella, D., Dietrich, S., et al. (2017). Observational analysis of an exceptionally intense hailstorm over the Mediterranean area: Role of the GPM core observatory, *Atmospheric Research*, *192*, 72–90, ISSN 0169-8095. https://doi.org/10.1016/j.atmosres.2017.03.019

Meegan, C., Lichti, G., Bhat, P. N., Bissaldi, E., Briggs, M. S., Connaughton, V., et al. (2009). Thefermigamma-ray Burst Monitor. *The Astrophysical Journal*, *702*(1), 791–804. https://doi.org/10.1088/0004-637X/702/1/791

Østgaard, N., Neubert, T., Reglero, V., Ullaland, K., Yang, S., Genov, G., et al. (2019). First 10 months of TGF observations by ASIM. *Journal of Geophysical Research: Atmospheres*, *124*. https://doi.org/10.1029/2019JD031214

Panegrossi, G., Casella, D., Dietrich, S., Marra, A. C., Sano, P., Mugnai, A., et al. (2016). Use of the GPM constellation for monitoring heavy precipitation events over the Mediterranean region. *IEEE Journal of Selected Topics in Applied Earth Observations and Remote Sensing*, *9*, 2733–2753. https://doi.org/10.1109/JSTARS.2016.2520660

Pessi, A. T., & Businger, S. (2009). Relationships among lightning, precipitation, and hydrometeor characteristics over the North Pacific Ocean*. *Journal of Applied Meteorology and Climatology*, *48*, 833–848. https://doi.org/10.1175/2008jamc1817.1

Petersen, W. A., & Rutledge, S. A. (2001). Regional variability in tropical convection: Observations from TRMM. *Journal of Climate*, *14*, 3566–3586. https://doi.org/10.1175/1520-0442(2001)014<3566:rvitco>2.0.co;2

Petracca, M. (2018). *Studio dell' attività elettrica nelle nubi temporalesche ed utilizzo dei dati di fulminazione per la meteorologia operativa*. Ph.D thesis.

Prigent, C., Defer, E., Pardo, J. R., Pearl, C., Rossow, W. B., & Pinty, J.-P. (2005). Relations of polarized scattering signatures observed by the TRMM microwave instrument with electrical processes in cloud systems. *Geophysical Research Letters*, *32*, L04810. https://doi.org/10.1029/2004GL022225

Rakov, V. A., & Uman, M. A. (2003). *Lightning: Physics and effects*. Cambridge University Press. https://doi.org/10.1017/cbo9781107340886

Roberts, O. J., Fitzpatrick, G., Stanbro, M., McBreen, S., Briggs, M. S., Holzworth, R. H., et al. (2018). The first Fermi-GBM terrestrial gamma ray flash catalog. *Journal of Geophysical Research: Space Physics*, *123*(5), 4381–4401. https://doi.org/10.1029/2017JA024837

Rudlosky, S. D. (2015). Evaluating ENTLN performance relative to TRMM/LIS. *Journal of Operational Meteorology*, *3*(2), 11–20. https://doi.org/10.15191/nwajom.2015.0302

Rutledge, S. A., Petersen, W. A., Cifelli, R. C., & Carey, L. D. (2000). Early results from TRMM-LBA: Kinematic and microphysical characteristics of convection in distinct meteorological regimes. In *IEEE 2000 International Geoscience and Remote Sensing Symposium. Taking the Pulse of the Planet: The Role of Remote Sensing in Managing the Environment. Proceedings (Cat. No.00CH37120)* (Vol. 3, pp. 1358–1360). IEEE. https://doi.org/10.1109/IGARSS.2000.858118

Saunders, C. P. R., Keith, W. D., & Mitzeva, R. P. (1991). The effect of liquid water on thunderstorm charging. *Journal of Geophysical Research*, *96*(D6), 11007–11017. https://doi.org/10.1029/91jd00970

Seto, S., & Iguchi, T. (2015). Intercomparison of attenuation correction methods for the GPM Dual-frequency precipitation radar. *Journal of Atmospheric and Oceanic Technology*, *32*, 915–926. https://doi.org/10.1175/JTECH-D-14-00065.1

Shao, X.-M., Hamlin, T., & Smith, D. M. (2010). A closer examination of terrestrial gamma-ray flash-related lightning processes. *Journal of Geophysical Research*, *115*, A00E30. https://doi.org/10.1029/2009JA014835

Smith, D. M., Buzbee, P., Kelley, N. A., Infanger, A., Holzworth, R. H., & Dwyer, J. R. (2016). The rarity of terrestrial gamma-ray flashes: RHESSI stacking analysis. *Journal of Geophysical Research: Atmosphere*, *121*, 11382–11404. https://doi.org/10.1002/2016JD025395

Smith, D. M., Hazelton, B. J., Grefenstette, B. W., Dwyer, J. R., Holzworth, R. H., & Lay, E. H. (2010). Terrestrial gamma ray flashes correlated to storm phase and tropopause height. *Journal of Geophysical Research*, *115*, A00E49. https://doi.org/10.1029/2009JA014853

Smith, D. M., Lopez, L. I., Lin, R. P., & Barrington-Leigh, C. P. (2005). Terrestrial gamma-ray flashes observed up to 20 MeV. *Science*, *307*, 1085–1088. https://doi.org/10.1126/science.1107466

Speirs, P., Gabella, M., & Berne, A. (2017). A comparison between the GPM dual-frequency precipitation radar and ground-based radar precipitation rate estimates in the Swiss Alps and Plateau. *Journal of Hydrometeorology*, *18*, 1247–1269. https://doi.org/10.1175/JHM-D-16-0085.1

Spencer, R. W., Goodman, H. M., & Hood, R. E. (1989). Precipitation retrieval over land and ocean with the SSM/I: Identification and characteristics of the scattering signal. *Journal of Atmospheric and Oceanic Technology*, *6*, 254–273. https://doi.org/10.1175/1520-0426(1989)006<0254:prolao>2.0.co;2

Splitt, M. E., Lazarus, S. M., Barnes, D., Dwyer, J. R., Rassoul, H. K., Smith, D. M., et al. (2010). Thunderstorm characteristics associated with RHESSI identified terrestrial gamma ray flashes. *Journal of Geophysical Research*, *115*, A00E38. https://doi.org/10.1029/2009JA014622

Stanley, M. A., Shao, X. M., Smith, D. M., Lopez, L. I., Pongratz, M. B., Harlin, J. D., et al. (2006). A link between terrestrial gamma-ray flashes and intracloud lightning discharges. *Geophysical Research Letters*, *33*, L06803. https://doi.org/10.1029/2005GL025537

Stith, J. L., Dye, J. E., Bansemer, A., Heymsfield, A. J., Grainger, C. A., Petersen, W. A., & Cifelli, R. (2002). Microphysical observations of tropical clouds. *Journal of Applied Meteorology*, *41*, 97–117. https://doi.org/10.1175/1520-0450(2002)041<0097:mootc>2.0.co;2

Takahashi, T. (1978). Riming electrification as a charge generation mechanism in thunderstorms. *Journal of the Atmospheric Sciences*, *35*, 1536–1548. https://doi.org/10.1175/1520-0469(1978)035<1536:reaacg>2.0.co;2

Tavani, M., Barbiellini, G., Argan, A., Boffelli, F., Bulgarelli, A., Caraveo, P., et al. (2009). The AGILE mission. *Astronomy and Astrophysics*, *502*(3), 995–1013. https://doi.org/10.1051/0004-6361/200810527

Tiberia, A., Dietrich, S., Porcù, F., Marisaldi, M., Ursi, A., & Tavani, M. (2019). Gamma ray storms: Preliminary meteorological analysis of AGILE TGFs. *Rendiconti Lincei. Scienze Fisiche e Naturali*, *30*, 259–263. https://doi.org/10.1007/s12210-019-00775-y

Tierney, D., Briggs, M. S., Fitzpatrick, G., Chaplin, V. L., Foley, S., McBreen, S., et al. (2013). Fluence distribution of terrestrial gamma ray flashes observed by the Fermi Gamma-ray Burst Monitor. *Journal of Geophysical Research: Space Physics*, *118*, 6644–6650. https://doi.org/10.1002/jgra.50580

Todd, M. C., & Bailey, J. O. (1995). Estimates of Rainfall over the United Kingdom and surrounding seas from the SSM/I using the polarization corrected temperature algorithm. *Journal of Applied Meteorology*, *34*, 1254–1265. https://doi.org/10.1175/15200450(1995)034,1254:EOROTU.2.0.CO;2

Toracinta, E. R., Cecil, D. J., Zipser, E. J., & Nesbitt, S. W. (2002). Radar, passive microwave, and lightning characteristics of precipitating systems in the tropics. *Monthly Weather Review*, *130*, 802–824. https://doi.org/10.1175/1520-0493(2002)130,0802:RPMALC.2.0.CO;2

Ursi, A., Marisaldi, M., Dietrich, S., Tavani, M., Tiberia, A., & Porcù, F. (2019). Analysis of thunderstorms producing terrestrial gamma-ray flashes with the meteosat second generation. *Journal of Geophysical Research: Atmospheres*, *124*(23), 12667–12682.

Ushio, T., Heckman, S. J., Boccippio, D. J., Christian, H. J., & Kawasaki, Z.-I. (2001). A survey of thunderstorm flash rates compared to cloud top height using TRMM satellite data. *Journal of Geophysical Research*, *106*(D20), 24089–24095. https://doi.org/10.1029/2001JD900233

Virts, K. S., Wallace, J. M., Hutchins, M. L., & Holzworth, R. H. (2013). Highlights of a new ground-based, hourly global lightning climatology. *Bulletin of the American Meteorological Society*, *94*, 1381–1391. https://doi.org/10.1175/BAMS-D-12-00082.1

Weinman, J. A., & Guetter, P. J. (1977). Determination of rainfall distributions from microwave radiation measured by the Nimbus 6 ESMR. *Journal of Applied Meteorology*, *16*, 437–442. https://doi.org/10.1175/1520-0450(1977)016<0437:dordfm>2.0.co;2

Wentz, F. J., Ashcroft, P., & Gentemann, C. (2001). Post-launch calibration of the TRMM microwave imager. *IEEE Transactions on Geoscience and Remote Sensing*, *39*, 415–422. https://doi.org/10.1109/36.905249

Williams, E., Boldi, R., Bór, J., Sátori, G., Price, C., Greenberg, E., et al. (2006). Lightning flashes conducive to the production and escape of gamma radiation to space. *Journal of Geophysical Research*, *111*, D16209. https://doi.org/10.1029/2005JD006447

Williams, E. R. (1985). Large-scale charge separation in thunderclouds. *Journal of Geophysical Research*, *90*, 6013–6025. https://doi.org/10.1029/jd090id04p06013

Williams, E. R., Weber, M. E., & Orville, R. E. (1989). The relationship between lightning type and convective state of thunderclouds. *Journal of Geophysical Research*, *94*, 13213–13220. https://doi.org/10.1029/JD094iD11p13213

Zhu, Y., Rakov, V. A., Tran, M. D., Stock, M. G., Heckman, S., Liu, C., et al. (2017). Evaluation of ENTLN performance characteristics based on the ground truth natural and rocket-triggered lightning data acquired in Florida. *Journal of Geophysical Research: Atmospheres*, *122*(18), 9858–9866. https://doi.org/10.1002/2017jd027270

Zipser, E. J., & Lutz, K. R. (1994). The vertical profile of radar reflectivity of convective cells: A strong indicator of storm intensity and lightning probability? *Monthly Weather Review*, *122*, 1751–1759. https://doi.org/10.1175/1520-0493(1994)122<1751:tvporr>2.0.co;2